Full length article

Superconducting Cu/Nb nanolaminate by coded accumulative roll bonding and its helium damage characteristics

Rui Gao[a,b], Miaomiao Jin[b,c,*], Fei Han[b], Baoming Wang[d], Xianping Wang[a,*], Qianfeng Fang[a], Yanhao Dong[a], Cheng Sun[e], Lin Shao[f], Mingda Li[b], Ju Li[b,d,*]

[a] Key Laboratory of Materials Physics, Institute of Solid State Physics, Chinese Academy of Sciences, Hefei 230031, PR China
[b] Department of Nuclear Science and Engineering, Massachusetts Institute of Technology, Cambridge, MA 02139, United States
[c] Department of Fuels Modeling and Simulation, Idaho National Laboratory, Idaho Falls, ID 83415, USA
[d] Department of Materials Science and Engineering, Massachusetts Institute of Technology, Cambridge, MA 02139, United States
[e] Characterization and Advanced PIE Division, Idaho National Laboratory, Idaho Falls, ID 83415, USA
[f] Department of Nuclear Engineering, Texas A&M University, College Station, TX 77845, USA

ARTICLE INFO

ABSTRACT

A very broad distribution of microstructural length scales spanning few nm- to the μm-scale has proven effective to achieve exceptional materials properties. Here, we fabricate a Cu/Nb two-phase composite made of a hierarchically layered structure by modifying the conventional accumulative roll bonding (ARB) technique, where fresh Nb sheets are inserted and bonded during a repeated stacking and rolling process. This barcode-like multilayer with a designed hierarchical length scale distribution possesses densely distributed phase boundaries and rich interfacial structures. The composite demonstrates similar superconductivity characteristics as pure Nb, but is 3 × stronger, has theoretically better oxidation resistance, and retains considerable ductility. Under the helium irradiation environment, the unique interfacial structures featuring chemical intermixing zones (3-dimensional) are more immune to the formation of large helium clusters than atomically sharp interfaces (2-dimensional), screening them from radiation damage and improving their long-term mechanical integrity. This work signifies an effective strategy of constructing hierarchical laminates to achieve high-performance materials, which holds promise in fusion and fission energy applications.

© 2020 Published by Elsevier Ltd on behalf of Acta Materialia Inc.

1. Introduction

Manipulating microstructural length scales is a well-utilized design strategy to optimize materials properties, such as the trade-off between strength and ductility of metallic alloys [1]. Severe plastic deformation (SPD) including equal channel angular pressing (ECAP) [2], high-pressure torsion (HPT) [3] and accumulative roll bonding (ARB) [4], can be used to refine grains and/or introduce layered structures to improve the strength of materials. In contrast to the *unimodal* grain sizes or multilayer spacing, recent studies demonstrated that a judicious combination of multiple characteristic dimensions in a material spanning from the nanoscale to the macroscale could be more effective to obtain a better-integrated behavior than a unimodal nanoscaled material [5,6]. For example, Ma and coworkers [7] reported a high ductility in a nanostructured Cu with a bimodal grain size distribution prepared by cold rolling and proper heat treatments, as the coarse microstructure sustains strain-hardening to stabilize tensile deformation while the fine part imparts strength. Lu [8] demonstrated a gradient microstructure introduced by surface mechanical attrition treatment with a variety of grain sizes, leading to a good strength-ductility tradeoff. Another example is multilayered structures where the ductility of cold-rolled Cu/Cu laminates nearly doubles that of cold-rolled Cu alone due to decreased necking facilitated by the laminated structure with a broad range of layer thicknesses ranging from 1.8 μm - 500 nm [9].

However, multi-scale materials with a certain portion of nano-sized grains could be unstable when exposed to extreme conditions encountered in nuclear fission or fusion, because smaller grain sizes contribute to a high driving force for recrystallization and/or abnormal grain growth under irradiation and thermal environment [10,11]. A single-phase structure can easily coarsen due to the high mobility of grain boundaries (GBs) via short-range diffusion, which degrades the long-term mechanical properties. To over-
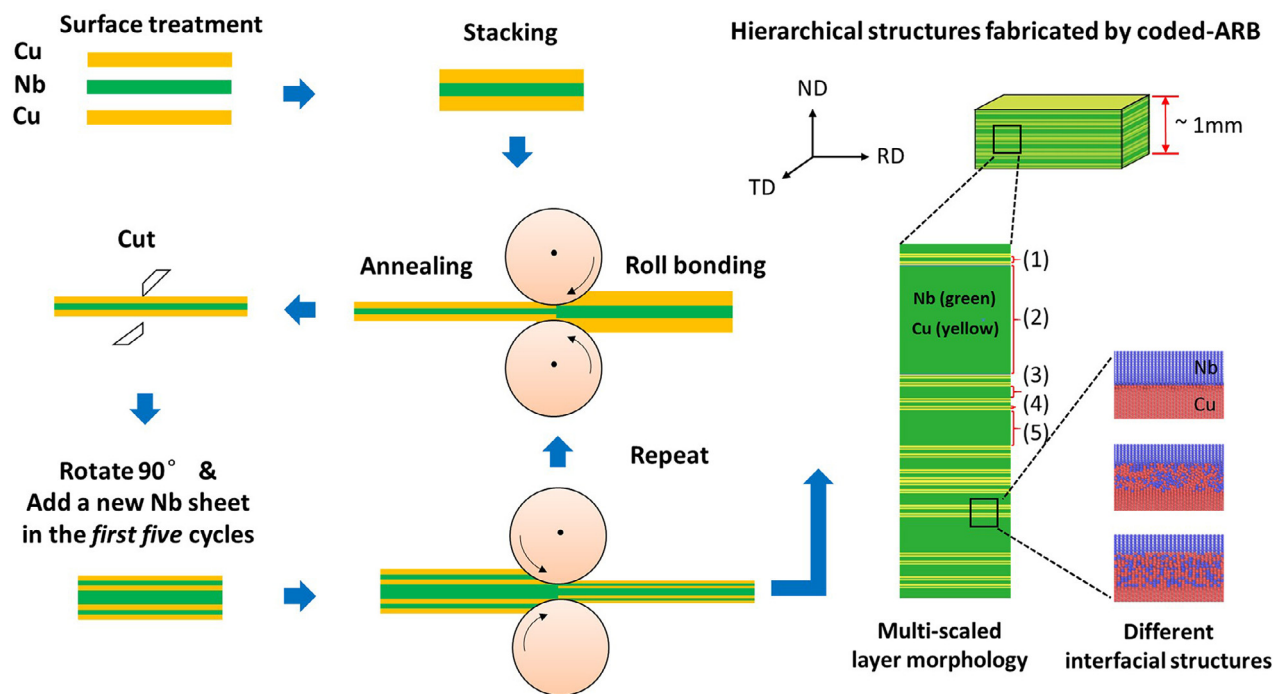
Fig. 1. Schematic illustration of the coded-ARB process. Hierarchical structures can be formed in the Cu/Nb composites after repetitive stacking, rolling, annealing and cut. Multi-scaled layered morphology and diverse interfacial structures closely depend on the number of Nb sheets added and rolling cycles.

come these issues, phase boundaries (PBs) of multilayer composites consisting of immiscible elements can be utilized to improve thermal stability and radiation tolerance. Such phase boundaries also provide ample sinks for radiation-induced defects [12–15], and generally require solute partitioning and long-range diffusion in order to move (except for massive phase transformations, which is not the case in this work).

Conventional ARB which involves repeated stacking and rolling of a starting bilayer or trilayer sheet is a highly efficient and low-cost process to fabricate those immiscible laminates [4]. A unimodal, nanolayered structure could be obtained after the repeatedly rolled sheet experiences extreme strain while preserving the overall bulk dimensions. For example, many studies have explored the potential applications of ARB Cu/Nb laminates with a regularly repeating structure in nuclear energy which requires the material to exhibit high strength [16,17] and excellent resistance to radiation [18], elevated temperature [12] and oxidation/corrosion [19]. Nb-based metals are the most commonly used superconductors in particle accelerators and fusion tokamaks [20,21] where the magnets undergo significant radiation damage. Especially, helium (He) as the transmutation product in nuclear reactors generally builds up in grain/phase boundaries (GBs/PBs) and significantly degrades mechanical performance. Additionally, magnet coils fabricated in the form of superconductor tape need to experience winding during fabrication and sustain huge Lorentz forces in service. Therefore, Cu/Nb laminates as functional material can prove useful in nuclear applications if superconductivity can be achieved along with the high yield strength, tolerable ductility and good irradiation resistance.

In this study, a hierarchical Cu_{FCC}/Nb_{BCC} nanolaminate with a morphology similar to the "barcode" is fabricated by repeatedly inserting fresh Nb layers during the modified ARB process. We take advantage of this technique to program arbitrary layer thicknesses ranging from a few nanometers to microns and diverse interfacial structures. The ultra-thin Cu layers embedded in the thick Nb lamellae with different layer thicknesses can prevent oxygen from penetrating Nb matrix (as oxygen is highly soluble and mobile in

Nb_{BCC} and degrades ductility rapidly [22], but the solubility and permeability in Cu_{FCC} are much less), and triple the yield strength, while preserving similar superconductivity properties as pure Nb. We also found that helium radiation damage resistance is drastically enhanced near specific types of interfaces, the mechanisms of which are elaborated via both helium implantation experiments and molecular dynamics (MD) simulations.

2. Experimental section

2.1. Sample fabrication

Fig. 1 depicts the fabrication of hierarchical Cu/Nb nanolaminates by the coded accumulative roll bonding (coded-ARB) technique. Firstly, commercial rolled Cu (99.95 wt.%) and Nb (99.99 wt.%) plates with a dimension of 20 mm (width) × 30 mm (length) × 1 mm (thickness) were annealed at 600 °C and 800 °C for 5 h in an ultra-high vacuum (10^{-5} Pa), respectively, to reduce dislocations from the machining process. Then, annealed Cu and Nb sheets assembled as a three-layer sandwich stack (Cu-Nb-Cu) were rolled at room temperature in air to reach about 70% reduction in total thickness, which is necessary to guarantee sufficient bonding between the Cu and Nb layers. Intermediate heat treatment of the rolled sandwiched structure was carried out at 600 °C for 1 h in a vacuum furnace after each rolling step. Then the annealed sheet was cut in half, stacked, and rotated 90° in the RD-TD plane as shown in the schematic. The thickness of the composite sheet was approximately 1 mm after every rolling cycle. Different from the conventional ARB process that maintains constant component during the rolling [23,24], as for our modified process, fresh Nb sheets of designed thickness were added as the interlayer during the initial few rolling cycles. Taking an example of five fresh Nb sheets added ("coding level" = 5), the final nominal composition is 70Nb-30Cu by weight. Except for the bonding between Cu and freshly added Nb during the initial 5 passes, the other subsequent combinations only involved bonding Cu to Cu, which prevents the oxidation of Nb layers during rolling in the air. In order to avoid re-

Table 1

As for Cu/Nb multilayers with the component of 70 wt% Nb and 30 wt% Cu, the nominal thickness of the multi-scaled layers with the number of rolling cycles.

Rolling cycles	Nominal thickness of the multi-scaled layers (nm) 70 wt% Nb–30 wt% Cu					
	Cu	Nb (1)	Nb (2)	Nb (3)	Nb (4)	Nb (5)
15	4	4	12	36	109	326
13	16	16	48	145	434	1302
11	64	64	193	579	1736	5208
9	257	257	772	2315	6944	20,833
7	1029	1029	3086	9259	27,778	83,333

arrangement of the interfacial atomic structures, the thermal treatment was not applied during the last three rolling cycles.

In this paper, all the characterization focused on the 70Nb-30Cu by weight nanolaminate after 15 rolling cycles unless otherwise specified. The nominal individual layer thicknesses were calculated assuming the equal thickness reduction rate in Nb and Cu layers during coded-ARB (Table 1). The layered morphology of Cu/Nb laminates was studied by scanning electron microscope (SEM, Sirion200, FEI, USA) combined with energy-dispersive X-ray spectroscopy (EDS).

2.2. Mechanical property and superconductivity characterization of Cu/Nb nano-multilayer composites

The strength and ductility of hierarchical Cu/Nb laminates at room temperature were examined by uniaxial tensile testing. The dogbone tensile specimens with gauge dimensions 5 mm × 1.5 mm × 0.75 mm were cut from the RD-TD plane in each bulk composite at different rolling cycles by electrical discharge machining. Such specimens maintain structural integrity after the cutting and subsequent mechanical polishing. Tensile tests were carried out parallel to the RD of samples using an Instron 3369 Dual Column Tabletop Testing System with a constant displacement rate of 0.1 mm/min. The displacement of tensile samples was measured by a strain gauge type extensometer. Every strain-stress curve is derived from the average of three replicate tests. Experimental details of the tensile test are described in the Supplementary Information.

The electrical resistivity at room temperature of initial annealed Cu and Nb plates are 2.26×10^{-8} $\Omega \cdot$ m and 2.02×10^{-7} $\Omega \cdot$ m, respectively. All the Cu/Nb samples for resistivity measurement are prepared with a size of 10 mm × 3 mm × 0.1 mm. Importantly, such tapes were annealed at 350 °C for 2 h in an ultra-high vacuum to relieve residual stress after mechanical polishing. The sample preparation method is elaborated in the Supplementary Information. The superconducting transition resistivity of pure Nb and Cu/Nb films was analyzed according to the resistance test that was performed with an AC bridge using the conventional four-probe method in the physical property measurement system (PPMs). These tests were carried out in a helium cryostat equipped with a superconducting solenoid providing fields up to 1.5 Tesla. The temperature was controlled in the range of 2–12 K with an accuracy of ± 1 mK. And the plane of rolling-normal directions of samples was perpendicular to the magnetic field. T_c was defined as the midpoints of the resistive transitions $R(T)$.

2.3. He ion implantation and post-irradiation examination

Bulk Cu/Nb laminates without annealing were subjected to 300 keV He ion irradiation with two fluences of 1×10^{17} ions/cm^2 and 5×10^{17} ions/cm^2 by using a 400 kV accelerator at Texas A&M University, which were noted as lower and higher dose irradiation in this paper, respectively. The irradiation was performed at room temperature with an accuracy of ± 10 °C. Helium concentra-

tion (4.2 at% and 21 at%, low and high dose, respectively) as a function of irradiation depth (~830 nm) is estimated by SRIM (Stopping and Range of Ions in Solids) software. The average threshold displacement energy of 29 eV for Cu and 41 eV for Nb are applied in the calculation, respectively. To investigate the evolution of interfacial structures and bubbles morphology during the irradiation, cross-sectional transmission electron microscope (TEM) lamellae were prepared by the lift-out technique using the FEI Helios Nanolab 600 Dual Beam System (FIB) at 30 kV followed by low energy cleaning at 2 kV. The microstructure was characterized using a JEOL 2010F TEM operated at 200 kV.

2.4. Molecular dynamics simulation of radiation damage and helium bubble formation

MD simulations with the LAMMPS package [25] are used to examine Cu/Nb interfacial evolution under helium irradiation. The atomic interactions are described by an EAM potential [26], which is smoothly joined to the ZBL potential [27] to accommodate high energy atomic collisions. We constructed three bi-crystal systems containing three types of interfaces. The orientation of Cu and Nb layers marked in Fig. 8 is consistent with the experimental observations, and the thickness of each layer is 10 nm. The configurations contain 235,926 atoms, with a dimension of 13.4 nm × 12.6 nm × 20 nm and periodic boundary conditions. Based on the sharp interface system, the interfacial transition zone (ITZ) is created by randomly mixing Cu and Nb atoms within the 2 nm thickness interfacial domains. To generate the amorphous interfaces, the following procedure is utilized: i) the 2 nm slabs are melted at 1600 K for 200 ps with the rest of the atoms fixed, gradually quenched to 650 K over a span of 200 ps, ii) the whole system is quenched from 650 K to 300 K over 200 ps; iii) the whole system is first relaxed at zero pressure for 30 ps, and then at constant volume for another 30 ps. Finally, the three types of configurations are prepared for the helium radiation study.

To mimic the radiation process, we applied a multi-cascade molecular dynamics (MD) simulation algorithm [28]. Specifically, random cascades induced by 5 keV primary knock-on atoms (PKAs) are sequentially introduced into the simulation box, and each cascade lasts around 30 ps until the system is adequately annealed to ambient temperature. The ambient environment is modeled by thermostating the box boundary at 300 K, so that the excess energy from the PKAs gets drained gradually from the MD supercell. The radiation damage can be estimated with the NRT formulation [29], and one can obtain the experimental dose level by increasing the number of PKAs with additional computational cost. To account for helium atoms implantation at around the experimental helium/dpa ratio, on average, two He atoms are randomly created in the simulation box along with each PKA, and this accumulated helium evolves naturally upon damage cascades. The evolving atomic configurations are used for tracking helium behavior. The visualization is performed with the OVITO package [30].
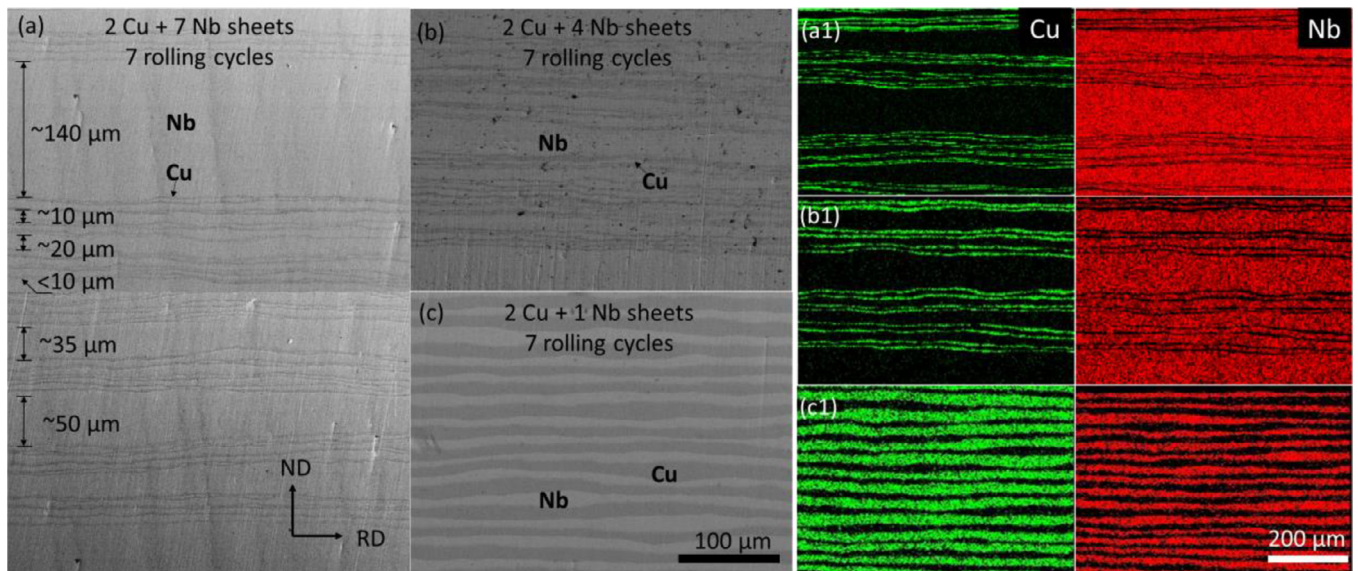
Fig. 2. The cross-sectional SEM images (a–c) and EDS mapping (a1–c1) of Cu/Nb multilayers with different components under the same rolling cycles. Different "barcode" structures, especially with highly variable Nb layer thicknesses, can be manipulated by the coded-ARB technique (a and b), compared to the homogeneous layered structure with nearly equal thickness prepared by traditional ARB (c). Scale bars in (a–c) are 100 μm and (a1–c1) are 200 μm, respectively.

3. Results

3.1. Microstructure characterization

3.1.1. Multi-scale layered morphology

As the Cu and Nb layers must undergo the same areal expansion to avoid delamination or rupture during rolling, and as plastic deformation conserves volume, the thickness ratio of all layers is preserved before and after rolling (assuming no mechanically driven intermixing). Thus, our only chances to modify the thickness distribution and phase fraction are by inserting fresh Nb layer of certain thickness after stacking and before roll-bonding step. How much fresh Nb we choose to insert each time is the "coding" part of coded-ARB. On one hand, the programed insertion or "code" controls the local stress/strain field inside the bulk to maintain layer integrity (detailed in the discussion section), and on the other hand, it can produce hierarchical structures to optimize properties.

Fig. 2 compares the secondary electron-SEM images (a–c) and EDS mapping (a1–c1) of layer morphology of Cu/Nb multilayers after the same 7 rolling cycles using current manufacturing strategy and conventional ARB. When inserting seven and four fresh Nb sheets during the coded-ARB process (Fig. 2a and b), the layer morphology becomes similar to "barcodes". It demonstrates that "barcode" structures, especially with highly variable Nb layer thicknesses taken up at different "coding levels", can be manipulated with the coded-ARB technique, compared to a homogeneous layered structure with nearly equal thickness prepared by traditional ARB (Fig. 2c). From these images, the interfaces are wavy and the layers remain continuous without fracture. Nb itself is very ductile in an oxygen-free environment, but can strain-harden significantly and quickly become brittle in the presence of oxygen [22]. However, the Cu layers can reduce oxygen permeation during rolling, so that even our nanoscale Nb layers maintain excellent deformability (Fig. 3a). Element distribution maps as shown in Fig. 2a1 and b1 demonstrate the multi-scale, heterogeneous structures in these composites with highly varying Nb layer thicknesses as different numbers of Nb sheets are added (see supplementary Table S1 for the distribution of nominal layer thickness). Moreover, diverse barcode structures can be also controlled by changing rolling cycles when the composition is fixed (see Supplementary Fig. S1).

After 15 rolling cycles (Fig. 3a), the thicknesses of both Cu phase and Nb phase can be reduced to the nanoscale. The nanoscaled "barcode" layered structure we obtained is uniform (see Fig. 3a), meaning that the layer thickness is almost constant at different in-plane locations with minimal deviation, hence, we performed a single measurement for the thickness of each layer in the direction perpendicular to the interfaces. Two TEM foils were lift-out at a depth of about 7 μm and 15 μm from the polished surface by focused ion beam (FIB), respectively, and for each foil, five TEM images with a magnification of 30,000 were captured with an order from top to bottom. The total measurements we have done to get the distribution of the layer thickness is around 800, i.e. from 800 different layers. The distribution statistics of Cu and Nb layers thickness is shown in Fig. 3b. About 57% of layers drop below 10 nm thick, while only 6% of layers are more than 100 nm thick. The fraction of layers distributed within 10–50 nm, 50–100 nm is 22% and 15%, respectively. Almost all the Cu layers are less than 10 nm thick. In addition, although the number of thick Nb layers is small, the total thickness of such layers whose thickness exceeds 100 nm occupies at least 100 μm in a 1mm-thick sample, illustrating the fractal-like morphology of our samples.

3.1.2. Diverse interfacial structures

In the case of highly variable layer thickness, interfacial structures become complex due to the shear instability driven by deformation and layer incompatibility, say, occurring between a very thin Cu layer and a very thick Nb layer. Here we distinguish three types of interfaces based on their atomic structures: atomically sharp interface, interfacial transition zone (ITZ), and amorphous zone (AMO). It has been observed that a large fraction of interfaces are relatively straight at a low magnification. As indicated in high-resolution images (Fig. 3d), some interfaces with well-defined lattice orientation relationships (OR) are atomically sharp due to the immiscible nature between neighboring Cu and Nb phases. Irregular zones representing chemical intermixing interfaces are indicated in Fig. 3e, where they look smeared and usually appear on either side of an ultra-thin layer with thicknesses less than 10 nm. And an FFT image obtained from a HRTEM image of this Nb layer was inserted. Fig. 3f shows a HRTEM image of interfaces with the crystallographic orientation relationship (OR) [112] $_{Cu}$ || [110] $_{Nb}$. At the sharp interface plane, the close-packed planes of
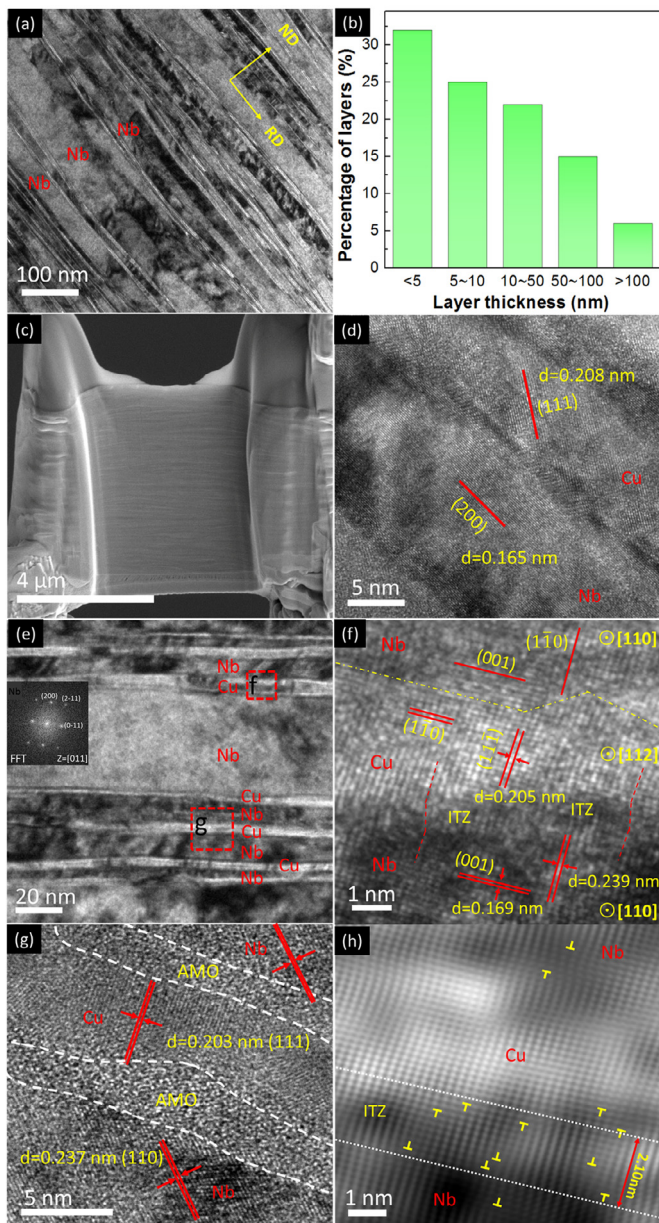
Fig. 3. (a) Representative cross-sectional TEM image obtained from nano-lamellar Cu/Nb multilayers prepared by coded-ARB. (b) The statistics of multi-scaled layer thickness distribution from two TEM lamellae (c) prepared by the focused ion beam. (d) High-resolution (HR) TEM image of an atomically sharp interface with a random orientation. (e) Low magnification image of typical morphology of intermixing interfaces and adjacent layers (inset is the FFT image obtained from this Nb layer). The rectangles are enlarged in (f) and (g), which show the interfacial transition zone (ITZ) and amorphous (AMO) interface, respectively. (h) Corresponding IFFT image of (f).

{111} in Cu and {110} in Nb follow the OR of $(11\bar{1})$ Cu $\parallel$ $(1\bar{1}0)$ $_{Nb}$. This OR for lattice direction and plane normal was also reported elsewhere [31]. However, the two planes rotate slightly in the ITZs where lattice constants deviate from the original values after undergoing SPD. In addition, the inverse fast Fourier transform (IFFT) pattern (Fig. 3h) of the ITZs in Fig. 3f shows clear lattice distortion and many misfit dislocations within a width of 2 nm. Furthermore, an amorphous phase of ~3 nm in width appears in the region between ultra-thin Nb and Cu layers with curved boundaries as shown in Fig. 3g. Such chemical intermixing zones have been reported in other bi-metal multilayers such as Cu/Nb [32], Cu/V [33], Cu/Zr [34], and Cu/Fe [35].

3.2. Mechanical behavior and superconductivity characterization

Fig. 4a shows the tensile engineering stress-strain curves of hierarchical Cu/Nb laminates with different rolling cycles. For comparison, the stress-strain curves of initially annealed Cu and Nb plates are illustrated as well. In general, ultimate tensile strength (UTS) monotonously increases with rolling cycles but the total elongation (TE) degrades gradually (Fig. 4b). After 15 rolling cycles, the UTS of 584 MPa is about 2.8 times that of pure Cu or Nb. Although the reduction of TE is dramatic compared to pure Cu and Nb, the total elongation of nearly 10% in these laminates still exhibits satisfactory performance for the superconducting magnet winding process. The fracture surfaces after tensile tests indicate increasing brittleness as rolling cycle increases and thinner layers are produced (Supplementary Fig. S2).

The superconducting behavior of alloys or composites is significantly influenced by the constituent elements and microstructure. Nb is a typical type-II superconductor. For use in superconducting magnets, not only the superconducting transition temperature T_c, but also the upper and lower critical magnet fields and the critical current density, are key metrics [36]. Here, the superconductivity metrics of hierarchical Cu/Nb multilayers (after 15 rolling cycles) are compared with those of pure Nb and annealed Cu/Nb multilayers (annealed at 800 °C for 3 h, where the lamellar microstructure breaks down into equiaxed grains, Supplementary Fig. S3). Fig. 5a–c shows the T_c of three samples via measuring superconducting transition resistivity and their upper critical magnetic field (H_{c2}) extrapolated by Ginzburg-Landau fitting (Fig. 5d). At zero magnetic field, the resistivity of the three materials shows a sharp transition and their T_c is almost the same at around 9 K, demonstrating that both kinds of Cu/Nb multilayer composites possess similar superconductivity to pure Nb. With increasing magnetic field, T_c of all three materials shifts toward lower temperatures, but the T_c of hierarchical Cu/Nb multilayer and the annealed one decreases faster, especially in strong magnetic fields. Different from the hierarchical morphology in coded-ARB composite, a high density of grooves in the annealed composite introduced by transformed equiaxed grains increase the boundary scattering and suppress its superconductivity [37]. The hierarchical Cu/Nb sample achieves a higher T_c than the annealed one for the magnetic field above 0.6 Tesla. This trend is more obvious at higher magnetic fields due to the enhanced pinning effect of chemical intermixing interfacial structures on magnetic flux lines [38]. In conclusion, our coded-ARB Cu/Nb composite achieves a similar superconducting-electrical-current load capability as pure Nb, but with nearly 3 × tensile strength and satisfactory ductility, which properties satisfy the basic engineering requirement as steady magnetic field magnets.

3.3. Helium radiation damage tuned by interfacial structures

While coarse-grained unimodal materials are susceptible to embrittlement by helium segregation at the GBs [39], in the presence of well-dispersed, stabilized PBs that serve as plentiful helium interstitial sinks, the sharp interface networks are "screened" and the degradation of mechanical performance in hierarchical materials can be significantly reduced. The helium dynamics in these hierarchical laminates is demonstrated under both low and high dose helium irradiation.

3.3.1. Lower dose helium irradiation

We carried out a series of *ex situ* helium ion implantation experiments at room temperature (RT) to investigate the helium radiation response. Fig. 6a shows the helium distribution across the irradiated region under the lower fluence of 10^{17} He ions/cm^2. It
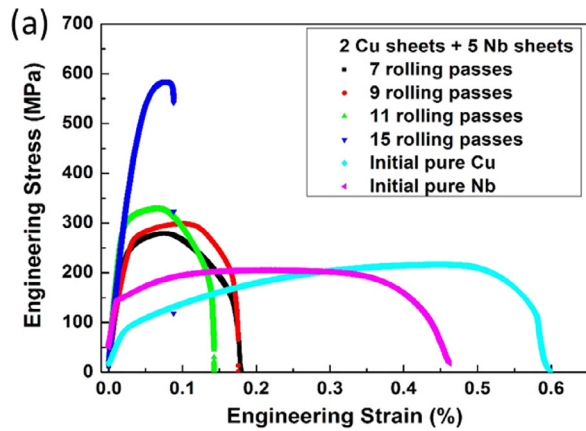
Fig. 4. (a)Tensile engineering stress-strain curves for the bulk pure Cu, pure Nb, and coded-ARB Cu/Nb nanolaminates with different rolling cycles. (b) The ultimate tensile strength (UTS) and tensile elongation (TE) of the pure Cu, pure Nb and coded-ARB Cu/Nb nanolaminates with different rolling cycles, respectively.
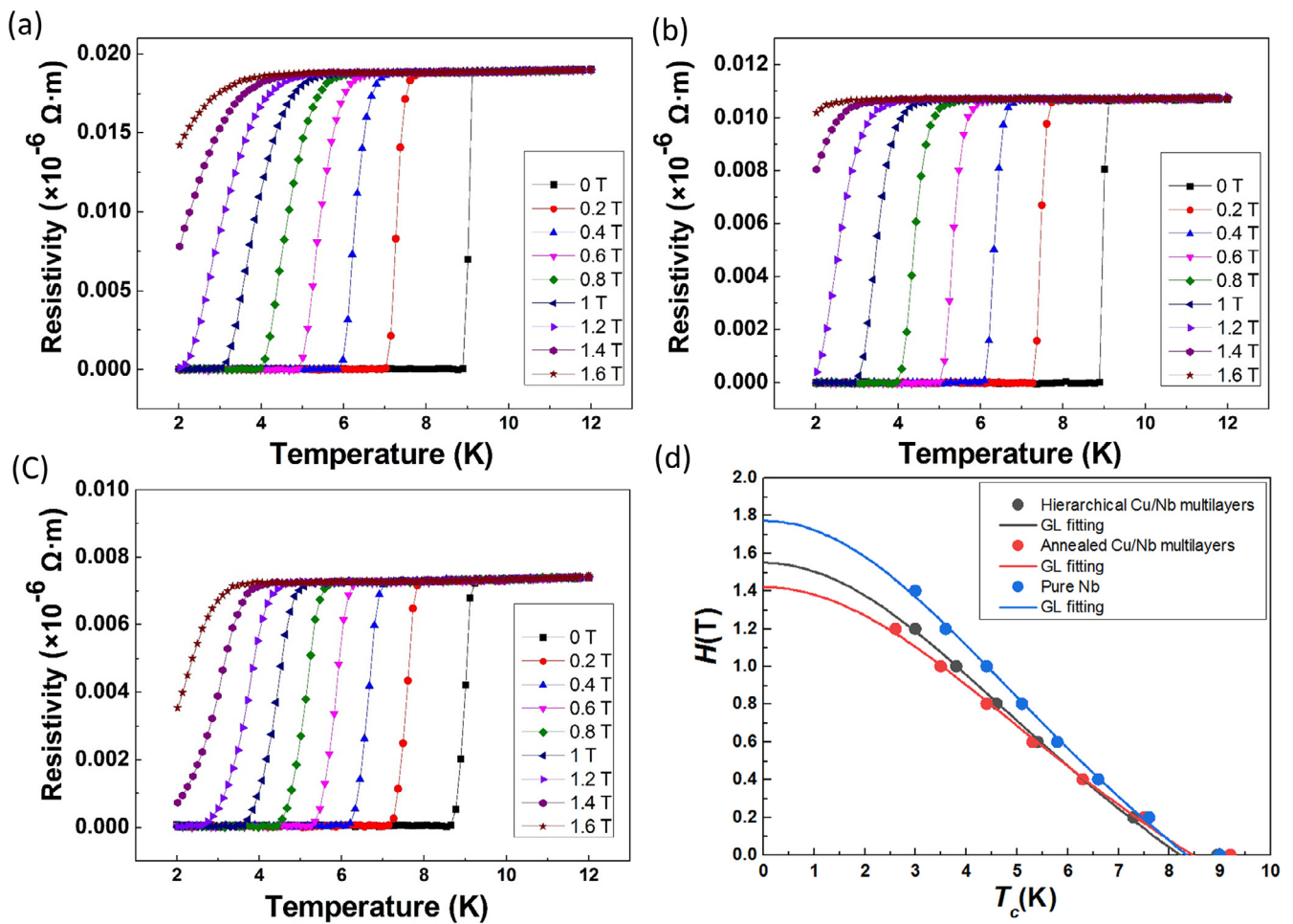
Fig. 5. Resistivity superconducting transitions of (a) hierarchical Cu/Nb multilayers, (b) annealed Cu/Nb multilayers, and (c) pure Nb at different magnetic fields. (d) Phase diagram of the critical field derived from the resistivity transition curves. The superconducting transition temperatures (T_c) of hierarchical Cu/Nb multilayers (black), annealed Cu/Nb multilayers (red), and pure Nb (blue) are presented as solid circles. The solid line shows the theoretical curve fit based on the Ginzburg-Landau theory. (For interpretation of the references to color in this figure legend, the reader is referred to the web version of this article.)

can be seen that a large number of tiny bubbles exist within 500–800 nm from the surface. The peak helium concentration is about 4 at% according to the SRIM (Stopping and Range of Ions in Solids) calculation [40]. Except for some bubbles as bright white spots preferentially located in the Cu layers (Fig. 6b), other ones also regularly align as spindle-shaped channels at the sharp interface as shown in Fig. 6c, demonstrating a phase-boundary wetting char-

acteristic [41,42]. In contrast, helium precipitates distributed in the intermixing regions are more isolated, exhibiting no helium bubble alignment. Fig. 6d illustrates that some separate bubbles with a diameter of ~0.7 nm are embedded fully inside the Cu layer near the amorphous zone, but bubbles are hardly observed by HRTEM in the amorphous zone or near crystalline-amorphous interface from the Nb side (denoted as the bubble denuded zone, or BDZ). Fig. 6e
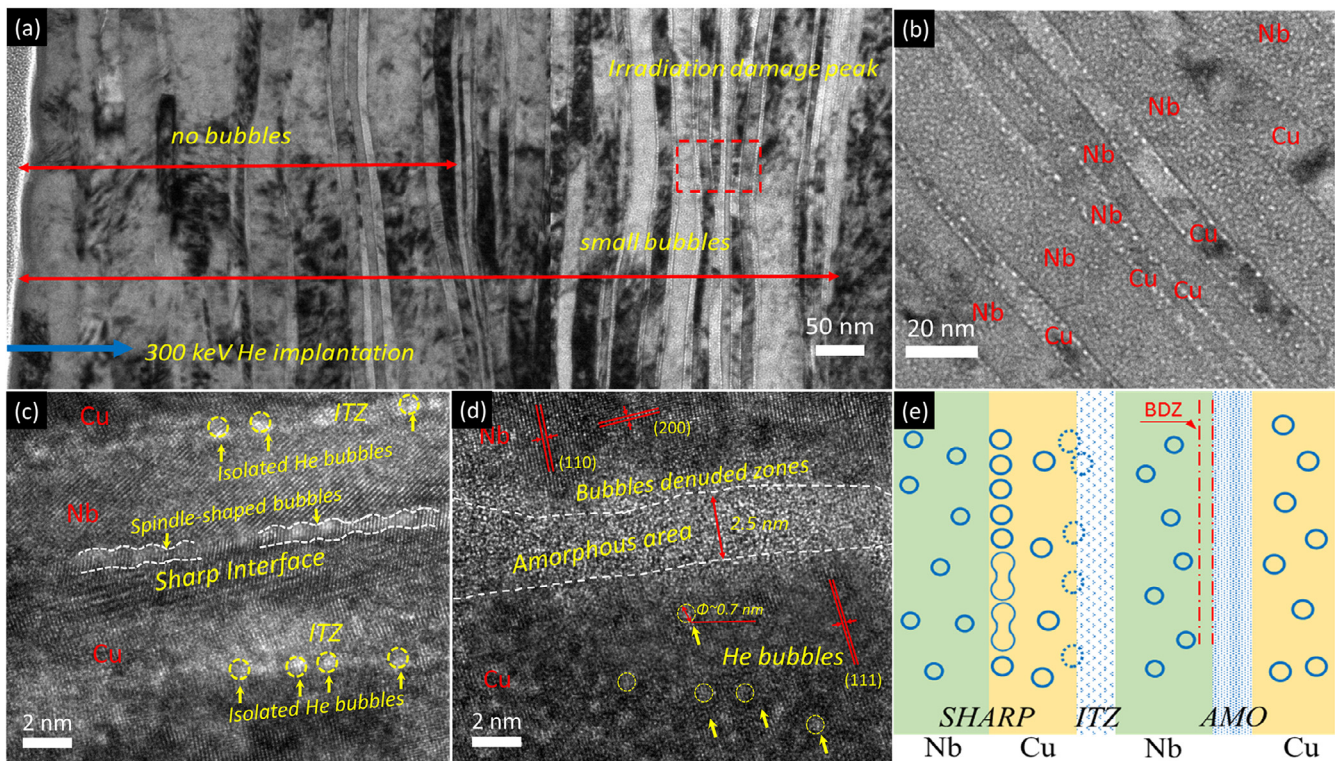
Fig. 6. Under a He irradiation dose of 10^{17} ions/cm^2, (a) a typical cross-section TEM image showing the distribution of irradiation-induced bubbles within the helium implanted region. (b) Local enlarged region of the concentrated He bubbles, corresponding to the area marked with a red square in (a). HRTEM images of He bubble morphology in (c) sharp interfaces and interfacial transition zones, and (d) the amorphous area. (e) Schematic of helium bubble evolution as the function of interfacial structures according to the experimental observation, where BDZ stands for bubble denuded zone. (For interpretation of the references to color in this figure, the reader is referred to the web version of this article.)

schematically shows the evolution of helium bubbles at the three types of interfaces. ITZ and amorphous interfaces hinder the formation of large bubbles even under this extremely large dose of helium implantation (40,000 appm, one or two orders of magnitude larger than fusion vacuum vessel conditions at end of life) [43], in contrast to the sharp interfaces where helium bubble production is preferable. It is worth mentioning that the amorphous nature of these interfaces is still maintained after irradiation.

3.3.2. Higher dose helium irradiation

Fig. 7a indicates the microstructure of hierarchical Cu/Nb multilayers under a higher dose irradiation (5×10^{17} ions/cm^2). The majority of large bubbles grow in nanoscaled layers in the peak helium concentration region around 600–900 nm from the surface. The morphology of helium bubbles is dependent on the thickness of layers. Two areas with similar helium implantation are highlighted in Fig. 7b, and enlarged in Fig. 7c and d. One can see elongated bubbles confined by an ultra-thin layer about 8 nm in thickness (Fig. 7c). The contrast between yellow and blue dashed lines suggests that these bubbles coalesce in different depths of the TEM lamella. The HRTEM image shows large wetting angles of those equiaxed bubbles, which are not beneficial to the formation of continuous linear bubble channels according to the wetting theory [44]. Fig. 7d highlights that faceted cavities with a diameter of around 5 nm in the thick Cu layer adhere to interfaces instead of spanning across the entire layer, and are bounded by planes of $(111)_{Cu}$ and $(100)_{Cu}$, owing to the low free surface energies of 1.06 J/m^2 and 1.13 J/m^2, respectively [45]. It is apparent that the faceted bubble has a smaller wetting angle θ_2 compared to the equiaxed one θ_1, which makes them more likely to form extended bubble channels. Here, it is difficult to distinguish the character of sharp or ITZ interfaces in TEM images because of heavy radiation-

induced defects and pressurized bubble formation. Many spherical helium bubbles exist in the Cu layer near the general interface, but bubbles are still hardly visible in the adjacent regions next to a 3 nm wide amorphous area, which indicates the BDZs (Fig. 7e). This zone formation is attributed to the high sink efficiency of the amorphous interface for helium, accommodating helium interstitials with large excess free volume. In addition, the amorphous regions are stable even under higher irradiation damage and do not show radiation-induced devitrification (RID) as observed in other studies [46].

3.3.3. Molecular dynamics simulation of He damage

MD simulations are used to model the helium irradiation process by consecutively introducing PKAs with 5 keV kinetic energy and randomly placed helium atoms. The atomic configurations of the above three systems before irradiation and at a damage level of 1.5 DPA (displacements per atom) are depicted in Fig. 8. From the magenta shaded profiles showing the Cu distribution, it can be inferred that this mixing is inefficient due to the immiscible nature of Cu/Nb atoms. Relatively more Cu atoms mix into the Nb matrix because of the large atomic radius mismatch (12.1%, $r_{Nb} > r_{Cu}$) and the open structure of BCC Nb [32]. Irradiation causes damage to the initial interfacial structures: the sharp interface becomes smeared within a small width, while ITZ and amorphous interfaces change in composition, and become more similar in structure.

During irradiation, helium atoms are randomly introduced into the systems, and they tend to combine into clusters due to their thermodynamic immiscibility with metallic atoms [47]. From Fig. 8d–f, it can be seen that i) the interfacial regions contain the most helium clusters and ii) the Cu layer contains many more helium clusters than the Nb layer. The former is expected as the interface is an efficient sink for helium atoms. The latter is attributed
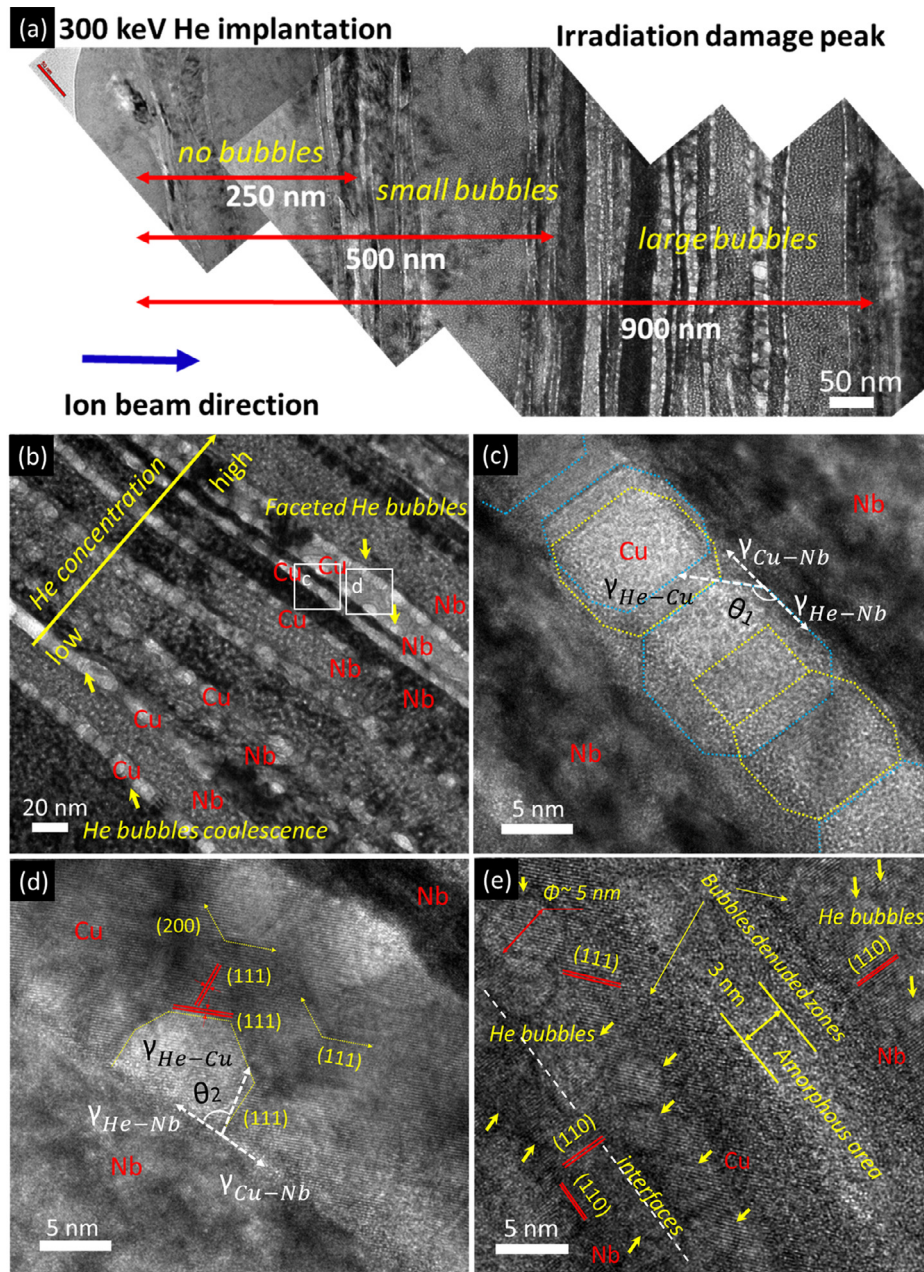
Fig. 7. Under a He irradiation dose of 5 × 10^{17} ions/cm^2, (a) TEM image of a helium implantation zone ranging from the surface to 900 nm. (b) Exhibiting the different helium bubbles morphology with helium concentration and layer thickness. (c-d) Bubble channels consisted of (c) overlapping equiaxed bubbles and (d) faceted bubbles with different wetting angles in the cross-section. (e) Helium bubbles with larger radii are located at the general interface, but the stable amorphous area does not exhibit visible bubbles in the TEM image. (For interpretation of the references to color in this figure, the reader is referred to the web version of this article.)

to the fact that relatively slow helium diffusion in FCC Cu is beneficial for interstitials to form small clusters [47]. In addition, competition between helium clustering and interface sinking contributes to the formation of a distinct denuded zone of helium clusters in the Nb bulk close to the interface, which is marked by the light yellow shaded band in Fig. 8d–f. Here, it should be mentioned that these MD simulations generate a dose rate several orders of magnitude higher than that in the experiments, which means long-timescale thermal diffusion is excluded. However, given realistic experimental conditions where the migration of vacancy and helium-vacancy complexes play an important role in mass transport either to the bulk or to interfaces, thereby, BDZs are also expected to appear in the Cu bulk as demonstrated in Fig. 7e. The helium cluster size distribution and helium density are quantified in different interfacial regions (Fig. 8g) and separate Cu and Nb layers

(Supplementary Fig. S4) after 1.5 DPA. The sharp interface which confines helium atoms in a quasi-2D zone, contains a higher density of helium interstitials and helium clusters than the other interfaces. By comparison, the amorphous and ITZ systems outperform the sharp interface system in terms of "capacity". Furthermore, although the concentration of helium atoms in Nb is slightly less than that in Cu, larger helium clusters usually exist in the Nb matrix (Fig. S4), which is attributed to the fast diffusion of helium in BCC Nb.

4. Discussions

When bi-metal composites laminates are rolled, the hard component is in tension and prone to necking along the rolling direction (RD) (Fig. 9a) [48,49]. In the current scenario, the Nb layer
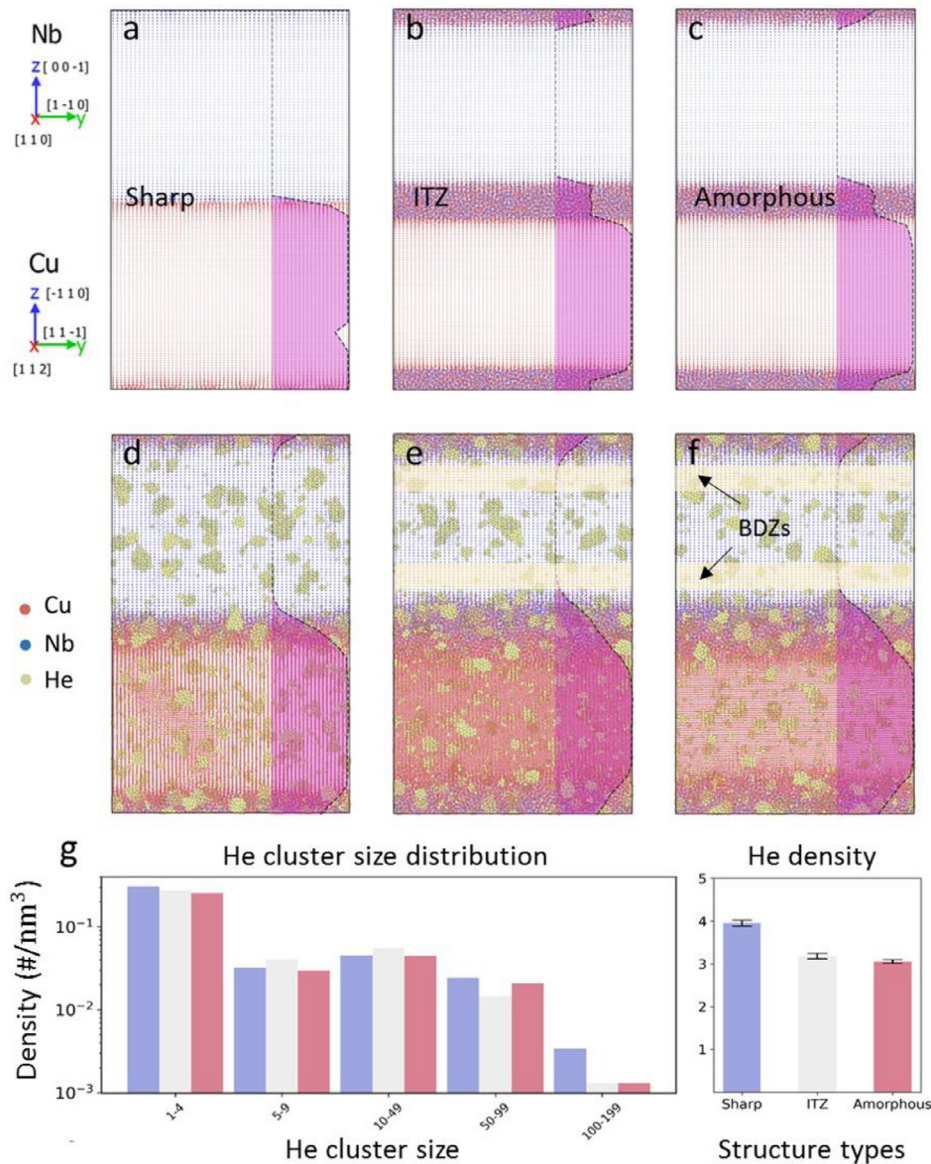
Fig. 8. Atomic configurations before (a–c) and after 1.5 DPA irradiation (d–f) at 300 K, with Cu atoms in red, Nb atoms in blue, and He atoms in yellow. Systems with three types of interfacial structures are depicted, including sharp interface (a and d), interfacial transition zone (ITZ, b and e), and amorphous interfaces (c and f). The magenta shaded profiles indicate the Cu atom distribution, demonstrating radiation-induced atom mixing near the interfaces. Notice that after helium implantation, all the interfacial regions shown in d–f are filled with helium clusters, and a distinct denuded zone (light yellow shadow) of the helium cluster appears in the Nb layer close to the interfaces. (g) Statistics of helium density and helium cluster size distribution in the different interfacial structures after irradiation. (For interpretation of the references to color in this figure legend, the reader is referred to the web version of this article.)

could gradually harden when deformation-induced defects can not be completely annihilated during the intermediate annealing due to a higher melting point of Nb (2468 °C). Therefore, the addition of fresh Nb sheets (annealed) accommodates the reduced ductility of hardened rolled sheets due to the layer refinement, e.g. unit 3 of new Nb sheet as a core and unit 1 of rolled sheets as skins in Fig. 9b, which increases the critical strain for necking and thus delays necking during the coded-ARB process [48]. Moreover, by constructing barcode units (Fig. 9c), one sectional shear strain near the thicker rolled Nb layers in the RD can be transformed into the compressive strain in the normal direction (ND) (Fig. 9c), similar to the hard-plate rolling process [50]. This variation of strain/stress field decreases the shear strain at interfaces, maintaining the layer integrity [50].

The formation mechanism of unique interfacial structures can be understood from the dislocation mediated diffusion process.

When the layer thickness is around a few microns during the coded-ARB, the dislocations uniformly glide within the whole layers and pile up at the interfaces. Few dislocations transmit through the sharp interfaces (Fig. 9d) due to the smaller stress. Once the layer thickness drops down to hundreds of nanometers and the total equivalent strain increases largely, activated misfit dislocations repeatedly transmit across a high density-interfaces, accelerating the mixing of the Cu atoms into the Nb lattice via "dislocation pumps [51]" (Fig. 9e) . Moreover, due to the reduction of vacancy formation energy under an ultra-large stress, the number of excess vacancies increases by a few orders of magnitude, promoting atomic transportation near the interfaces [35]. As the stored deformation energy increases upon accumulating plastic strain with a high density of lattice defects, such intermixing zones may even lead to amorphization [32,52,53]. In this work, the final maximum equivalent strain is as high as 14.3 in both the thinnest Cu and Nb
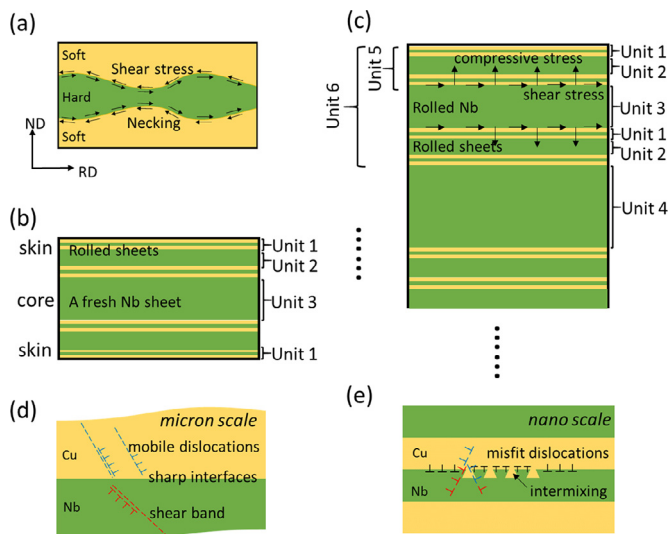
Fig. 9. (a) Schematic illustration of the stress field at the interface during rolling. (b) By adding a fresh Nb sheet, strength/hardness difference between a new sheet and rolled sheets decreases. (c) Stress field within layers changes via the construction of variable barcode units. (d) Plenty of mobile dislocations freely migrate within the micron scaled Cu and Nb layers and pile up at Cu/Nb sharp interfaces during the rolling. (e) Lattice misfit dislocations transmit through interfaces between nano-scaled layers by shear stress, leading to the mechanically induced chemical intermixing.

layers calculated by Eq. (1) [14], vastly increasing the possibility of formation of ITZs and amorphous zones. Since post-annealing at a high temperature could induce phase transformation of interfacial structures, annealing was not performed to rolled samples during the last three rolling cycles.

$$\varepsilon = \frac{2}{\sqrt{3}} \ln\left(\frac{H_0}{h}\right) \qquad (1)$$

where H_0 and h are initial and final layer thicknesses, respectively.

The strengthening mechanism is strongly dependent on the microstructural length scale. The relationship between strength and layer thickness over 100 nm or even a few microns usually follows the Hall-Petch relation [16]. In this case, dislocations mainly glide in thicker Nb layers and are blocked by interfaces. As layer thickness continues to decrease, dislocations pile-up at interfaces contributes to the strength enhancement as larger stress is required to facilitate dislocation crossing the interfaces [54,55]. When layer thickness is reduced to few nanometers or to tens of nanometers, dislocations are confined in individual layers and strengthening is related to bowing of single dislocations [56]. In addition, with chemical intermixing interfaces, dislocation migration can be further inhibited due to extra free volume [57]. It has been found that a high-density of Cu layers can enhance crack resistance by preventing cracks crossing from one thick Nb layer to another [9]. However, it was reported that the transition from strain hardening to shear softening occurs in the Cu layer when its thickness is less than 10 nm, which can weaken its crack-shielding effect and thus decreasing the ductility of composites [58].

Helium accumulation in materials undoubtedly degrades their mechanical properties. It has been recognized that the failure of a macroscopic component is not determined by the average flaw size, and the average concentration of helium atoms and vacancies, but by the size of the largest flaw [59]. The key engineering tactic to delay the GB/PB crack caused by helium bubble aggregation is to manipulate the interfacial structure so there is no abnormal bubble growth or coalescence. Helium behavior at interfaces is mainly determined by two competing factors, the interfacial sink efficiency and the diffusivity of helium within the in-

terface [60]. The former is mainly dominated by the property and density of interfaces, while the latter is influenced by additional factors such as irradiation dose, temperature, stress, and pressure in helium bubbles [60–62]. In the case of atomically sharp interfaces (e.g. Kurdjumov–Sachs (K–S) oriented interfaces), helium atoms located at the interfacial sinks prefer to cluster due to their rapid 2D diffusion [63], then grow into bubbles and finally coalesce into helium channels with increasing helium implantation. In the ITZs, a large number of deformation-induced misfit dislocations can weaken the long-distance migration of helium atoms by providing free volume (like dislocation intersections at K-S interfaces) for efficiently trapping interstitial helium [51,64]. Similarly, the disordered atomic structure resulting from the heavy chemical intermixing accumulates a large amount of "vacancy-like" free volume [65,66]. In such 3D regions, helium atoms migrate rapidly and disperse homogeneously into trapping sites, reducing their long-range migration. Hence, these 3D (ITZ and amorphous) zones enhance the nucleation density of helium clusters, but suppress their further growth in comparison with the atomically sharp interfaces. Such understanding agrees with the rare experimental observation of bubbles in these more diffuse interfaces with wider width ("3D interfaces", rather than atomically sharp "2D interfaces") since the cluster size may be maintained below the stable bubble nucleation size, especially under a lower helium fluence. This finding extends previous studies on the superior radiation damage tolerance using crystalline/amorphous interfaces in multilayers [67].

5. Conclusion

We have fabricated a hierarchical Cu/Nb laminate composite via a modified "coded" ARB technique with freshly added Nb, which exhibited a beneficial combination of high strength (3 × that of pure Nb), sufficient ductility (~10%), superconductivity (similar to pure Nb), and superior helium irradiation resistance. Hierarchical structures including multi-scale distributed layer thicknesses similar to barcodes and diverse heterogeneous interfacial structures are manipulated by programming the thickness sequence of freshly inserted Nb layers and strain/stress field during the rolling process. Moreover, by means of *ex situ* helium implantation experiments and atomistic simulations, we found that controlling interfacial structures can effectively tune helium dynamics. The sharp interface is more susceptible to the aggregation of helium atoms/clusters due to their 2D diffusion characteristics. Conversely, interfacial transition and amorphous zones significantly delay the formation of larger helium clusters because such 3D interfaces with excess free volume and high "sink capacity" for helium increase cluster nucleation but suppress their growth. This design principle based on severe plastic deformation processing could lead to enhanced structural and functional nuclear materials for extreme-environment applications.

Declaration of Competing Interest

The authors declare that they have no known competing financial interests or personal relationships that could have appeared to influence the work reported in this paper.

Acknowledgments

Supplementary materials

Supplementary material associated with this article can be found, in the online version, at doi:10.1016/j.actamat.2020.07.031.

References

[1] R.Z. Valiev, R.K. Islamgaliev, I.V. Alexandrov. Bulk nanostructured materials from severe plastic deformation, Prog. Mater. Sci. 45 (2000) 103.

[2] R.Z. Valiev, T.G. Langdon, Principles of equal-channel angular pressing as a processing tool for grain refinement, Prog. Mater. Sci. 51 (2006) 881–981.

[3] A. Zhilyaev, T. Langdon, Using high-pressure torsion for metal processing: fundamentals and applications, Prog. Mater. Sci. 53 (2008) 893–979.

[4] Y. Saito, H. Utsunomiya, N. Tsuji, T. Sakai, Novel ultra-high straining process for bulk materials—development of the accumulative roll-bonding (ARB) process, Acta Mater. 47 (1999) 579–583.

[5] E. Ma, X. Wu, Tailoring heterogeneities in high-entropy alloys to promote strength-ductility synergy, Nat. Commun. 10 (2019) 5623.

[6] U.G. Wegst, H. Bai, E. Saiz, A.P. Tomsia, R.O. Ritchie, Bioinspired structural materials, Nat. Mater. 14 (2015) 23–36.

[7] Yinmin Wang, Mingwei Chen, Fenghua Zhou, En Ma, High tensile ductility in a nanostructured metal, Nature 419 (2002) 912–915.

[8] K. Lu, Making strong nanomaterials ductile with gradients, Science 345 (2014) 1455–1456.

[9] H.S. Liu, B. Zhang, G.P. Zhang, Enhanced toughness and fatigue strength of cold roll bonded Cu/Cu laminated composites with mechanical contrast, Scr. Mater. 65 (2011) 891–894.

[10] N. Li, J. Wang, Y.Q. Wang, Y. Serruys, M. Nastasi, A. Misra, Incoherent twin boundary migration induced by ion irradiation in Cu, J. Appl. Phys. 113 (2013) 023501–023508.

[11] W.B. Liu, C. Zhang, Y.Z. Ji, Z.G. Yang, H. Zang, T.L. Shen, L.Q. Chen, Irradiation-induced grain growth in nanocrystalline reduced activation ferrite/martensite steel, J. Appl. Phys. 105 (2014) 121905.

[12] A. Misra, R.G. Hoagland, H. Kung, Thermal stability of self-supported nanolayered Cu/Nb films, Philos. Mag. 84 (2004) 1021–1028.

[13] W. Han, M.J. Demkowicz, N.A. Mara, E. Fu, S. Sinha, A.D. Rollett, Y. Wang, J.S. Carpenter, I.J. Beyerlein, A. Misra, Design of radiation tolerant materials via interface engineering, Adv. Mater. 25 (2013) 6975–6979.

[14] L.F. Zeng, R. Gao, Q.F. Fang, X.P. Wang, Z.M. Xie, S. Miao, T. Hao, T. Zhang, High strength and thermal stability of bulk Cu–Ta nanolamellar multilayers fabricated by cross accumulative roll bonding, Acta Mater. 110 (2016) 341–351.

[15] K. Kang, J. Wang, I.J. Beyerlein, Atomic structure variations of mechanically stable fcc-bcc interfaces, J. Appl. Phys. 111 (2012) 053531.

[16] C. Ding, J. Xu, X. Li, D. Shan, B. Guo, T.G. Langdon, Microstructural evolution and mechanical behavior of Cu/Nb multilayer composites processed by accumulative roll bonding, Adv. Eng. Mater. 22 (2019) 1900702.

[17] M.J. Demkowicz, L. Thilly, Structure, shear resistance and interaction with point defects of interfaces in Cu–Nb nanocomposites synthesized by severe plastic deformation, Acta Mater. 59 (2011) 7744–7756.

[18] L.X. Yang, S.J. Zheng, Y.T. Zhou, J. Zhang, Y.Q. Wang, C.B. Jiang, N.A. Mara, I.J. Beyerlein, X.L. Ma, Effects of He radiation on cavity distribution and hardness of bulk nanolayered Cu–Nb composites, J. Nucl. Mater. 487 (2017) 311–316.

[19] Y. Choi, T.W. Lim, S.I. Hong, Corrosion and mechanical behavior of copper-niobium nano-filamentary micro-composites for high performance electrical conductor wire, Acta Metall. Sin. 15 (2002) 154.

[20] S. Hao, L. Cui, H. Wang, D. Jiang, Y. Liu, J. Yan, Y. Ren, X. Han, D.E. Brown, J. Li, Retaining large and adjustable elastic strains of kilogram-scale Nb nanowires, ACS Appl. Mater. Interfaces 8 (2016) 2917–2922.

[21] K.J. Leonard, T. Aytug, A.A. Gapud, F.A.L. Iii, N.T. Greenwood, Y. Zhang, A.G. Perez-Bergquist, W.J. Weber, Irradiation response of next generation high temperature superconductors for fusion energy applications, Fusion Sci. Technol. 66 (2017) 57–62.

[22] P.J. Yang, Q.J. Li, T. Tsuru, S. Ogata, J.W. Zhang, H.W. Sheng, Z.W. Shan, G. Sha, W.Z. Han, J. Li, E. Ma, Mechanism of hardening and damage initiation in oxygen embrittlement of body-centred-cubic niobium, Acta Mater. 168 (2019) 331–342.

[23] J. Li, W. Lu, S. Zhang, D. Raabe, Large strain synergetic material deformation enabled by hybrid nanolayer architectures, Sci. Rep. 7 (2017) 11371.

[24] X. Wu, M. Yang, F. Yuan, G. Wu, Y. Wei, X. Huang, Y. Zhu, Heterogeneous lamella structure unites ultrafine-grain strength with coarse-grain ductility, Proc. Natl. Acad. Sci. USA 112 (2015) 14501–14505.

[25] S. Plimpton, Fast parallel algorithms for short-range molecular dynamics, J. Comput. Phys. 117 (1995) 1–19.

[26] A. Kashinath, M.J. Demkowicz, A predictive interatomic potential for He in Cu and Nb, Model. Simul. Mater. Sci. Eng. 19 (2011) 035007.

[27] D.A. Bromley, Treatise on Heavy-Ion Science, Springer, 2012.

[28] M. Jin, P. Cao, M.P. Short, Thermodynamic mixing energy and heterogeneous diffusion uncover the mechanisms of radiation damage reduction in single-phase Ni-Fe alloys, Acta Mater. 147 (2018) 16–23.

[29] M.J. Norgett, M.T. Robinson, I.M. Torrens, A proposed method of calculating displacement dose rates, Nucl. Eng. Des. 33 (1975) 50–54.

[30] A. Stukowski, Visualization and analysis of atomistic simulation data with OVITO–the open visualization tool, Model. Simul. Mater. Sci. Eng. 18 (2010) 015012.

[31] N.A. Mara, I.J. Beyerlein, Review: effect of bimetal interface structure on the mechanical behavior of Cu–Nb fcc–bcc nanolayered composites, J. Mater. Sci. 49 (2014) 6497–6516.

[32] D. Raabe, S. Ohsaki, K. Hono, Mechanical alloying and amorphization in Cu–Nb–Ag in situ composite wires studied by transmission electron microscopy and atom probe tomography, Acta Mater. 57 (2009) 5254–5263.

[33] Siyuan Wei, Lifeng Zhang, Shijian Zheng, Xianping Wang, Jiangwei Wang, Deformation-induced interfacial transition zone in Cu/V nanolamellar multilayers, Scr. Mater. 159 (2019) 104–108.

[34] S. Ohsaki, S. Kato, N. Tsuji, T. Ohkubo, K. Hono, Bulk mechanical alloying of Cu–Ag and Cu/Zr two-phase microstructures by accumulative roll-bonding process, Acta Mater. 55 (2007) 2885–2895.

[35] L.F. Zhang, R. Gao, B.L. Zhao, M. Sun, K. Jing, X.P. Wang, T. Hao, Z.M. Xie, R. Liu, Q.F. Fang, C.S. Liu, Effects of annealing temperature and layer thickness on hardening behavior in cross accumulative roll bonded Cu/Fe nanolamellar composite, J. Alloys Compd. 827 (2020) 154312.

[36] U. Welp, Z.L. Xiao, J.S. Jiang, V.K. Vlasko-Vlasov, S.D. Bader, G.W. Crabtree, J. Liang, H. Chik, J.M. Xu, Superconducting transition and vortex pinning in Nb films patterned with nanoscale hole arrays, Phys. Rev. B 66 (2002) 212507.

[37] C.S.A. Sidorenko, T. Trappmann, H. v. Lo¯hneysen, Superconducting properties of fractal Nb/Cu multilayers, Phys. Rev. B 53 (1996) 11751.

[38] Peidong Yang, C.M. Lieber, Nanorod-superconductor composites: a pathway to materials with high critical current densities, Science 273 (1996) 1836–1840.

[39] X. Zhang, K. Hattar, Y. Chen, L. Shao, J. Li, C. Sun, K. Yu, N. Li, M.L. Taheri, H. Wang, J. Wang, M. Nastasi, Radiation damage in nanostructured materials, Prog. Mater. Sci. 96 (2018) 217–321.

[40] R.E. Stoller, M.B. Toloczko, G.S. Was, A.G. Certain, S. Dwaraknath, F.A. Garner, On the use of SRIM for computing radiation damage exposure, Nucl. Instrum. Methods Phys. Res. Sect. B: Beam Interactions Mater. Atoms 310 (2013) 75–80.

[41] D.V. Yuryev, M.J. Demkowicz, Modeling growth, coalescence, and stability of helium precipitates on patterned interfaces, Model. Simul. Mater. Sci. Eng. 25 (2017) 015003.

[42] D. Chen, N. Li, D. Yuryev, J. Wen, K. Baldwin, M.J. Demkowicz, Y. Wang, Imaging the in-plane distribution of helium precipitates at a Cu/V interface, Mater. Res. Lett. 5 (2017) 335–342.

[43] M.R. Gilbert, S.L. Dudarev, D. Nguyen-Manh, S. Zheng, L.W. Packer, J.C. Sublet, Neutron-induced dpa, transmutations, gas production, and helium embrittlement of fusion materials, J. Nucl. Mater. 442 (2013) S755–S760.

[44] N. Li, M.J. Demkowicz, N.A. Mara, Microstructure evolution and mechanical response of nanolaminate composites irradiated with helium at elevated temperatures, JOM 69 (2017) 2206–2213.

[45] S. Zheng, S. Shao, J. Zhang, Y. Wang, M.J. Demkowicz, I.J. Beyerlein, N.A. Mara, Adhesion of voids to bimetal interfaces with non-uniform energies, Sci. Rep. 5 (2015) 15428.

[46] J.Y. Zhang, Y.Q. Wang, X.Q. Liang, F.L. Zeng, G. Liu, J. Sun, Size-dependent He-ir-radiated tolerance and plastic deformation of crystalline/amorphous Cu/Cu–Zr nanolaminates, Acta Mater. 92 (2015) 140–151.

[47] A.Y. Dunn, M.G. McPhie, L. Capolungo, E. Martinez, M. Cherkaoui, A rate theory study of helium bubble formation and retention in Cu–Nb nanocomposites, J. Nucl. Mater. 435 (2013) 141–152.

[48] F. Nowicke, A. Zavaliangos, H.C. Rogers, The effect of roll and clad sheet geometry on the necking instability during rolling of clad sheet metals, Int. J. Mech. Sci. 48 (2006) 868–877.

[49] J.S. Carpenter, R.J. McCabe, S.J. Zheng, T.A. Wynn, N.A. Mara, I.J. Beyerlein, Processing parameter influence on texture and microstructural evolution in Cu-Nb multilayer composites fabricated via accumulative roll bonding, Metal. Mater. Trans. A 45 (2014) 2192–2208.

[50] H.Y. Wang, Z.P. Yu, L. Zhang, C.G. Liu, M. Zha, C. Wang, Q.C. Jiang, Achieving high strength and high ductility in magnesium alloy using hard-plate rolling (HPR) process, Sci. Rep. 5 (2015) 17100.

[51] E. Rabkin, Y. Estrin, Pipe diffusion along curved dislocations: an application to mechanical alloying, Scr. Mater. 39 (1998) 1731–1736.

[52] T.L. Wang, J.H. Li, K.P. Tai, B.X. Liu, Formation of amorphous phases in an immiscible Cu–Nb system studied by molecular dynamics simulation and ion beam mixing, Scr. Mater. 57 (2007) 157–160.

[53] C. Borchers, T. Al-Kassab, S. Goto, R. Kirchheim, Partially amorphous nanocomposite obtained from heavily deformed pearlitic steel, Mater. Sci. Eng.: A 502 (2009) 131–138.

[54] J. Wang, R.G. Hoagland, J.P. Hirth, A. Misra, Atomistic modeling of the interaction of glide dislocations with "weak" interfaces, Acta Mater. 56 (2008) 5685–5693.

[55] J.T. Avallone, T.J. Nizolek, B.B. Bales, T.M. Pollock, Creep resistance of bulk copper–niobium composites: an inverse effect of multilayer length scale, Acta Mater. 176 (2019) 189–198.

[56] J.Y. Zhang, F.L. Zeng, K. Wu, Y.Q. Wang, X.Q. Liang, G. Liu, G.J. Zhang, J. Sun, Size-dependent plastic deformation characteristics in He-irradiated nanostructured Cu/Mo multilayers: competition between dislocation-boundary and dislocation-bubble interactions, Mater. Sci. Eng.: A 673 (2016) 530–540.

[57] J.Y. Zhang, G. Liu, J. Sun, Self-toughening crystalline Cu/amorphous Cu-Zr nanolaminates: deformation-induced devitrification, Acta Mater. 66 (2014) 22–31.

[58] J.Y. Zhang, S. Lei, Y. Liu, J.J. Niu, Y. Chen, G. Liu, X. Zhang, J. Sun, Length scale-dependent deformation behavior of nanolayered Cu/Zr micropillars, Acta Mater. 60 (2012) 1610–1622.

[59] N.M. Pugno, R.S. Ruoff, Quantized fracture mechanics, Philos. Mag. 84 (2004) 2829–2845.

[60] H. Trinkaus, B.N. Singh, Helium accumulation in metals during irradiation – where do we stand? J. Nucl. Mater. 323 (2003) 229–242.

[61] I.J. Beyerlein, M.J. Demkowicz, A. Misra, B.P. Uberuaga, Defect-interface interactions, Prog. Mater. Sci. 74 (2015) 125–210.

[62] W.Z. Han, M.J. Demkowicz, E.G. Fu, Y.Q. Wang, A. Misra, Effect of grain boundary character on sink efficiency, Acta Mater. 60 (2012) 6341–6351.

[63] A. Kashinath, A. Misra, M.J. Demkowicz, Stable storage of helium in nanoscale platelets at semicoherent interfaces, Phys. Rev. Lett. 110 (2013) 086101.

[64] B.B. Straumal, B. Baretzky, A.A. Mazilkin, F. Phillipp, O.A. Kogtenkova, M.N. Volkov, R.Z. Valiev, Formation of nanograined structure and decomposition of supersaturated solid solution during high pressure torsion of Al–Zn and Al–Mg alloys, Acta Mater. 52 (2004) 4469–4478.

[65] R.E. Baumer, M.J. Demkowicz, Radiation response of amorphous metal alloys: subcascades, thermal spikes and super-quenched zones, Acta Mater. 83 (2015) 419–430.

[66] T.K. Chaki, J.C.M. Li, Radiation damage in an amorphous lennard-jones solid a computer simulation, Philos. Mag. B 51 (2006) 557–565.

[67] M. Jin, P. Cao, M.P. Short, Achieving exceptional radiation tolerance with crystalline-amorphous nanocrystalline structures, Acta Mater. 186 (2020) 587–596.

Supplementary Information

Superconducting Cu/Nb nanolaminate by coded accumulative roll bonding and its helium damage characteristics

Rui Gao, Miaomiao Jin*, Fei Han, Baoming Wang, Xianping Wang*, Qianfeng Fang, Yanhao Dong, Cheng Sun, Lin Shao, Mingda Li, Ju Li*

Experimental details

1. Tensile tests of Cu/Nb nano-multilayer composites:

Tensile specimens were cut into a small gauge size to get more samples from one bulk composite sheet, which avoids the difference in the mechanical behavior of composites from different batches.

The dogbone specimens with gauge dimensions 5 mm × 1.5 mm × 0.75 mm were cut from the RD-TD plane in each bulk composite with different rolling cycles by the electrical discharge machine (EDM). The ultra-thin metal molybdenum wire (diameter of 150 um) was used to cut the tensile sample with a very low step rate. And liquid coolant was splashed around samples to prevent overheating during the EDM process. In addition, because ARBed samples are relatively hard, all the specimens are integrated without any deformation during the cutting and subsequent mechanical polishing. Tensile tests were carried out parallel to the RD of samples using an Instron 3369 Dual Column Tabletop Testing System with a constant displacement rate of 0.1 mm/min. The displacement was measured by a strain gauge typed extensometer. The displacement of tensile sample was measured by a strain gauge typed extensometer. Every strain-stress curve is derived from the average of three replicate tests.

2. 4-point probe testing:

All the Cu/Nb composites samples for resistivity are prepared with a size of 10 mm×3 mm×0.1 mm. Because the reliable resistivity data could be measured from a thinner film when using 4-point probe testing in physical property measurement system (PPMs), thereby, such films were gently mechanically polished to 100 μm in thickness without obvious deformation and then annealed at 350 °C for 2 hours to relieve residual stress. The above processes are performed to prevent the effects of sample fabrication on data accuracy as much as possible.

Table S1. The nominal layer thickness of hierarchical structures in Cu/Nb composites with different components under seven rolling cycles.

Number of Nb sheets	Components	Nominal thickness in the multi-scaled layers (nm) (under 7 rolling cycles)							
		Cu	Nb (1)	Nb (2)	Nb (3)	Nb (4)	Nb (5)	Nb (6)	Nb (7)
1	*32 wt% Nb-68 wt% Cu*	3850	3850						
4	*66 wt% Nb-34 wt% Cu*	1543	1543	4630	13889	41667			
7	*76 wt% Nb-24 wt% Cu*	457	457	1372	4115	12346	37037	111111	333333
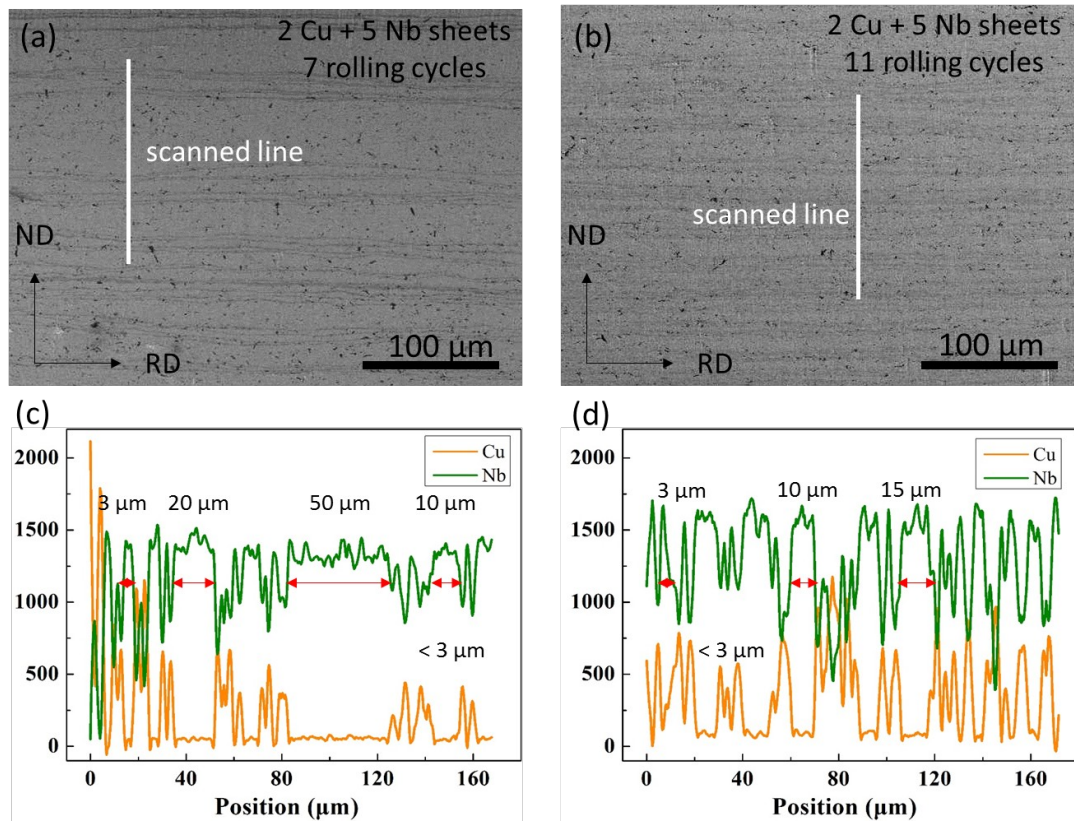
Figure S1. (a, b) SEM micrographs of hierarchical structures in Cu/Nb bulk composites (2 Cu + 5 Nb sheets) after 7 and 11 rolling cycles, respectively. (c, d) Corresponding elements distribution of EDS line scan analysis. There are at least five scales of hierarchical structures in this sample with 7 rolling cycles. The thickness distribution of Nb layers ranges around 50, 20, 10, 3 μm, and the thickness of Cu layers should be less than 3μm according to elements distribution of EDS line scan analysis (Fig. 3c). As for 11 rolling cycles, the distribution range of layer thickness seems to be less diverse due to the low resolution in SEM.
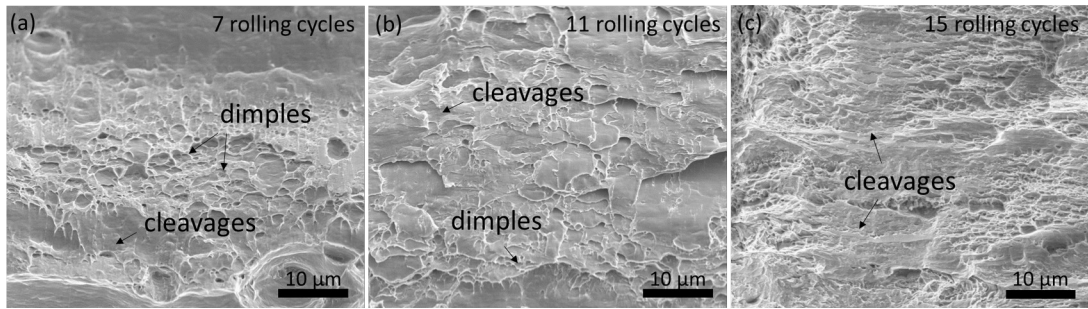
Figure S2. Fracture surfaces of samples after 7, 11 and 15 rolling cycles, respectively. Except for a few cleavages, large areas of typical dimple features are observed in samples with 7 and 11 rolling cycles, which represent the coexistence of brittle and ductile fracture. With increasing rolling cycles (Figure S2c), a large volume fraction of cleavages instead of dimples appear in a flat fracture surface. It is consistent with the high strength and limited ductility of Cu/Nb nanolaminates with ultra-thinner layers.
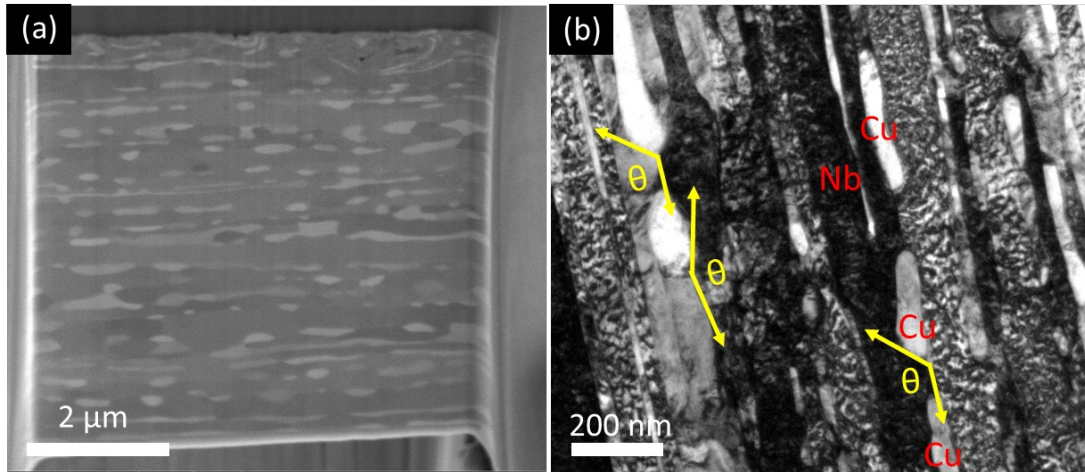
Figure S3. (a)A TEM foil sample of annealed Cu/Nb multilayers (annealed at 800°C for 3 hours) prepared by the FIB. (b) Cross-sectional TEM image of the annealed Cu/Nb composite, multilayer structure almost disappears and gradually transforms into equiaxed grains.
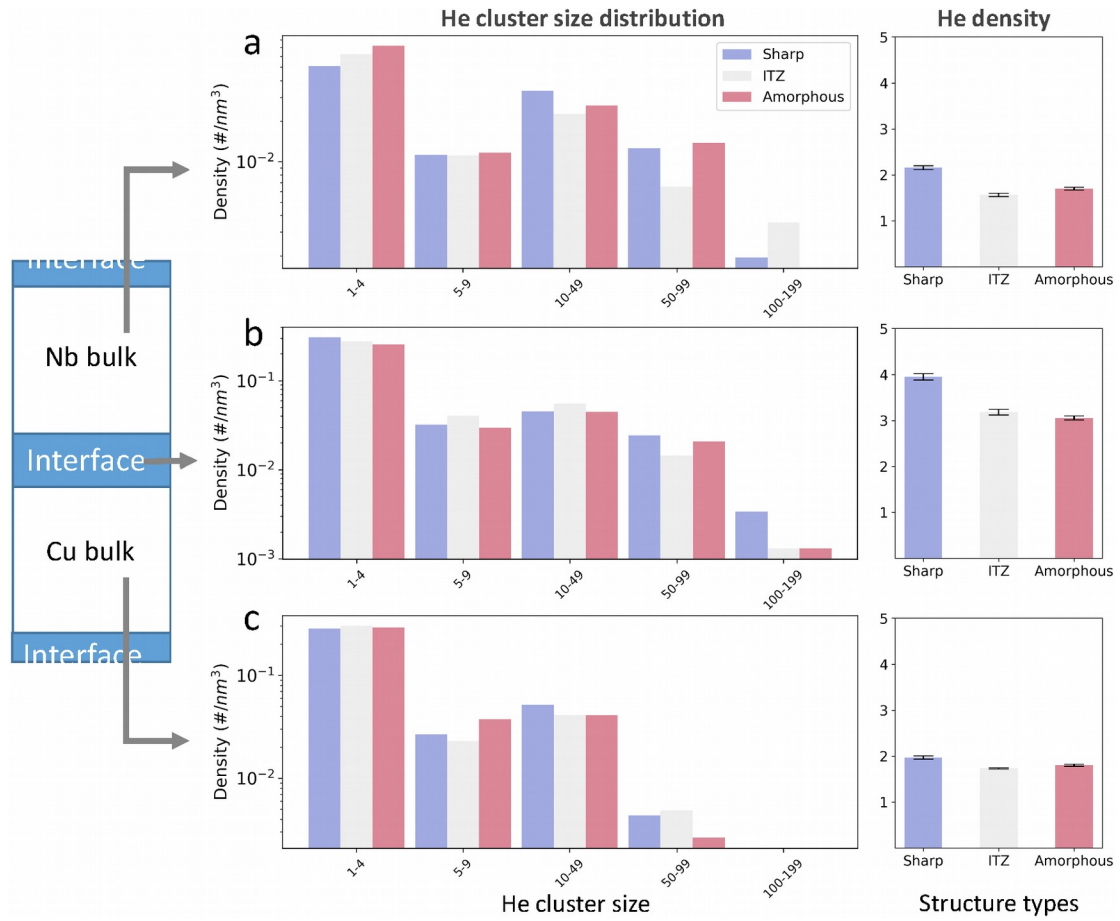
Figure S4. Helium cluster size distribution and helium density in three separate regions, i.e. Cu bulk (a), Nb bulk (b), and interfacial region (c) for three structural systems, after irradiation to 1.5 dpa at 300 K. All types of interfaces prefer to trap helium clusters, however, amorphous and ITZ ones are more immune to large clusters than sharp interfaces. Cu and Nb matrix also host He clusters, but with less density than that in interfaces. By comparison, Nb matrix has less but larger He clusters than that in Cu matrix due to a higher helium diffusivity in BCC-Nb. The total He density also confirms that interfaces are excellent sinks for helium clustering, while the sharp interface has a higher helium density than other interfaces. Overall, the ITZ and amorphous region with a larger volume provide more nucleation sites for clustering and dispersion of helium.